2026 IEEE International Conference on Robotics and Automation (ICRA 2026)
June 1-5, 2026. Vienna, Austria

CoPaRo: A Compact, Backdrivable 6-DOF Hybrid Parallel Robot with Serial-Like Form Factor and Large Workspace*

Samuel Verret and Clément Gosselin[1]

***Abstract*— A novel, compact, backdrivable 6-degree-of-freedom (DOF) hybrid parallel robot with a large axisymmetric workspace is proposed, referred to as CoPaRo, short for Compact Parallel Robot. The architecture achieves a high workspace-to-footprint ratio comparable to that of serial robots. The proposed robot is well suited for physical human-robot interaction (pHRI) due to its low inertia, backdrivability, and large workspace. A complete kinematic analysis is provided, including forward and inverse kinematics and velocity equations. All singularity conditions of the proposed architecture are identified, and the complete usable workspace is presented, accounting for singularities, mechanical interferences, and numerical stability. A CAD model and computer animations of the robot are provided to illustrate its motion, highlighting both the compact footprint and the large workspace. The actuators are positioned close to the base and transmit motion to distal joints via pulleys to reduce the robot's inertia. Direct-drive or quasi-direct-drive actuators can be used to enable backdrivability.**

I. Introduction

Physical human-robot interaction (pHRI) occurs when humans and robots come into direct contact, exchanging forces or motion. This interaction allows the complementary strengths of humans and robots to be combined: robots provide strength and repeatability, while humans offer adaptability. Effective pHRI requires the robot to respond smoothly and intuitively to forces applied by the human. Robot guidance can be achieved either through force/torque (F/T) sensors [1][2], which directly measure the forces and torques applied by the human, or by inferring these forces from actuator currents or joint displacements [3][4]. The use of F/T sensors is more common, particularly in industrial cobots [5], as it does not require the robot to be backdrivable. In non-backdrivable robots, relying solely on actuator measurements is ineffective because high gearing reduces the reflected force at the actuator, rendering it difficult to detect against noisy current signals. While F/T sensors enable interaction without backdrivability, they can reduce the intuitiveness of the interaction because the interaction bandwidth is limited, making the response less fluid. In contrast, backdrivable robots provide low reflected inertia and allow the joints to yield mechanically. This mechanical compliance increases the interaction bandwidth and results in more intuitive, fluid interactions [6], as the human perceives minimal resistance before the controller intervenes. Backdrivable joints are challenging to implement in serial robots due to the high actuator torques required to support the mass of the robot, its actuators, and its payload. An ideal robot for pHRI should combine low inertia and backdrivability to ensure safety and enable fluid interaction, while also providing a large translational and orientational workspace.

Parallel robots offer several advantages for pHRI, including high speed, acceleration, rigidity, accuracy, and payload capacity, as well as low inertia. However, they often suffer from a limited workspace and a large footprint compared to serial robots, which reduces their practical usefulness. The large footprint is largely due to the need to accommodate all actuators on the base. The limited workspace arises from type II singularities, leg interferences, and the overlapping constraints of each leg's reachable workspace, which become more restrictive as the number of legs increases. Kinematic redundancy can be employed to improve workspace by using the extra degrees of freedom to avoid singular configurations, as demonstrated in [7]-[9]. However, this approach requires additional actuators, increasing cost and, if the mechanism is not fully parallel, adding to the moving inertia. Another approach to enlarging the workspace is designing an axisymmetric workspace [10]-[12], achievable when the axes of each leg are coaxial, allowing rotation about a common axis and yielding a workspace similar to that of serial robots.

The Colibri [13] is a 6-DOF hybrid parallel robot featuring a two-leg architecture with the first joint of each leg positioned coaxially, enabling a large axisymmetric workspace. However, the platform employs a screw joint, which introduces mechanical complexity, friction, and backlash. Friction in the screw resists backdriving, reducing joint compliance and making pHRI less fluid and intuitive. Moreover, achieving large rotations with the limited linear displacement of the screw requires a small lead, which increases friction and can even make the system self-locking, further compromising backdrivability. Therefore, a trade-off exists between orientational workspace and backdrivability.

The goal of the research presented here is to develop a parallel or hybrid parallel robot with a large translational and orientational workspace, a small footprint, and backdrivable joints. To achieve this, a leg architecture similar to that of the Colibri robot can be retained to exploit its axisymmetric properties, while a novel platform architecture is designed to close the kinematic loop, improve backdrivability, and enlarge the orientational workspace, which in the Colibri is reported as 45° in tilt and 360° in torsion, although no singularity analysis was presented.

The paper is organized as follows. Section II presents

*The financial support of the Natural Sciences and Engineering Research Council of Canada (NSERC) is gratefully acknowledged, [Grant DG89715]

[1]The authors are with the Department of Mechanical Engineering, Université Laval, Québec, QC, Canada samuel.verret.1@ulaval.ca gosselin@gmc.ulaval.ca

a detailed description of the novel robot architecture. Sections III and IV address the inverse and forward kinematics, respectively. The velocity equations are developed in Section V, enabling a complete singularity analysis presented in Section VI. The translational and orientational workspace of the robot is presented in Section VII. Section VIII presents a virtual prototype, accompanied by computer animations to illustrate the robot's motion and highlight its large workspace.

II. Robot Architecture

The architecture of the proposed 6-DOF hybrid parallel robot consists of a moving platform connected to the base through two kinematically distinct legs, as illustrated in Fig. 1. Leg 1 is composed of an $\underline{\mathrm{R}}\underline{\mathrm{R}}\underline{\mathrm{R}}\mathrm{S}$ chain, shown in light gray in Fig. 1. Here, $\underline{\mathrm{R}}$ denotes an actuated revolute joint and S represents a passive spherical joint. The first actuated revolute joint is attached to the base, as indicated by the dashed lines in Fig. 1. Subsequently, two actuated revolute joints with parallel axes are mounted in series. Together, these three actuated revolute joints allow spatial positioning of the spherical joint of leg 1.

Leg 2 consists of an $\underline{\mathrm{R}}\underline{\mathrm{R}}\underline{\mathrm{R}}\mathrm{RRR}$ chain, shown in neutral gray in Fig. 1. Here, R denotes a passive revolute joint. The first three actuated revolute joints are arranged in the same configuration as in leg 1. A passive revolute joint is then mounted immediately after the last actuated joint, with its axis parallel to it. This is followed by two additional passive revolute joints mounted in series, each with its axis perpendicular to that of the preceding passive joint.

Leg 1 connects to the moving platform through its passive spherical joint, while leg 2 attaches via its last passive revolute joint. This arrangement closes the kinematic loop, linking the base to the moving platform through both legs. Shown in dark gray in Fig. 1, the moving platform forms a single continuous link, extending from the passive spherical joint of leg 1, passing through the passive revolute joint of leg 2, and terminating at the gripper. The gripper, depicted in Fig. 1 for illustrative purposes, is not functional; it merely indicates where an actuated gripper would be mounted.

Most of the variables describing the geometric architecture of the robot are illustrated in Fig. 2. The origin of the fixed base frame O_{xyz} is located on the axis of the first actuated revolute joint of leg 2. Two reference frames are attached to the moving platform: $O''_{x''y''z''}$ has its origin located at the centre of the passive spherical joint and $O'_{x'y'z'}$ has its origin located at the centre of the gripper. Both frames share the same orientation and differ only in position. Frame $O'_{x'y'z'}$ is used to facilitate the solution of the inverse kinematics, while $O''_{x''y''z''}$ simplifies the velocity equations and singularity analysis. In Fig. 2, l_{ij} $(i = 1, 2;\ j = 1, \ldots, 7)$ denotes the length of the j^{th} link of the i^{th} leg. Vector $\mathbf{u}_{i,j}$, defined along link j of leg i, has length $l_{i,j}$. The k^{th} joint angle of leg i is denoted by $\theta_{i,k}$. All vectors are expressed in the base frame of reference unless otherwise specified, except for $\mathbf{t}_b$ $(b = 1, 2, 3)$ which is expressed in the end-effector's reference frame. For conciseness, the following shorthand notation is used throughout this paper:

$$\mathrm{s}_{i,j} = \sin(\theta_{i,j}),\ \ \mathrm{c}_{i,j} = \cos(\theta_{i,j}),\ \ \mathrm{s}_{i,jk} = \sin(\theta_{i,j} + \theta_{i,k}),$$
$$\mathrm{c}_{i,jk} = \cos(\theta_{i,j} + \theta_{i,k}),\quad \mathrm{s}_{i,jkl} = \sin(\theta_{i,j} + \theta_{i,k} - \theta_{i,l}).$$

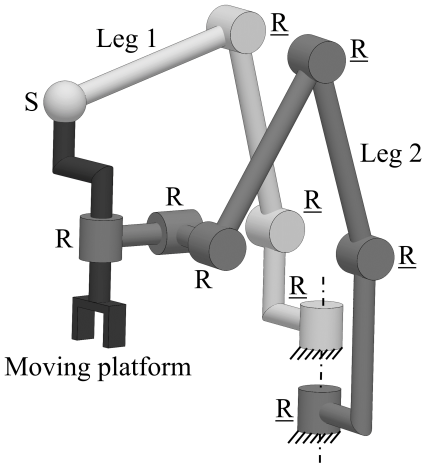

Fig. 1. Architecture of the proposed 6-DOF hybrid parallel robot.

III. Inverse Kinematics

The inverse kinematic problem is separated into two subproblems, one for each serial leg.

A. Leg 1

Since leg 1 is a spatial 3-DOF positioning mechanism, its inverse kinematics can be readily solved once $\mathbf{r}_1$ is known. Assuming the position and orientation of the end-effector, $\mathbf{p}$ and $\mathbf{Q}$, are given, $\mathbf{r}_1$ can be computed as

$$\mathbf{r}_1 = \mathbf{p} - \mathbf{u}_{1,0} + \mathbf{Q}\mathbf{t}_1. \tag{1}$$

With $\mathbf{r}_1$ determined, the inverse kinematic problem can be formulated with respect to this vector. We start by expressing the forward kinematics as

$$\mathbf{r}_1 = \mathbf{a}_{1,1} + \mathbf{Q}_{1,1}\mathbf{a}_{1,2} + \mathbf{Q}_{1,1}\mathbf{Q}_{1,2}\mathbf{a}_{1,3}. \tag{2}$$

where $\mathbf{Q}_{i,j}$ and $\mathbf{a}_{i,j}$ represent, respectively, the rotation matrix that brings frame (i, j) to frame $(i, j + 1)$ and the position vector connecting the origin of frame (i, j) to that of frame $(i, j+1)$, with both quantities expressed in frame i. A linear combination of the first two rows of (2), weighted by $\mathrm{s}_{1,1}$ and $\mathrm{c}_{1,1}$, yields an equation of the form

$$A\,\mathrm{s}_{1,1} + B\,\mathrm{c}_{1,1} + C = 0, \tag{3}$$

where

$$A = r_{1,x}, \qquad B = -r_{1,y}, \qquad C = l_{1,1},$$

and $r_{1,x}$ and $r_{1,y}$ denote the first and second components of $\mathbf{r}_1$, respectively. Equation (3) is a well known standard form that yields two solutions for $\theta_{1,1}$, obtained using the tangent of the half-angle substitution.

Next, rearranging all three rows of $\mathbf{r}_1$ and then taking the sum of the squares of these rows yields an equation of

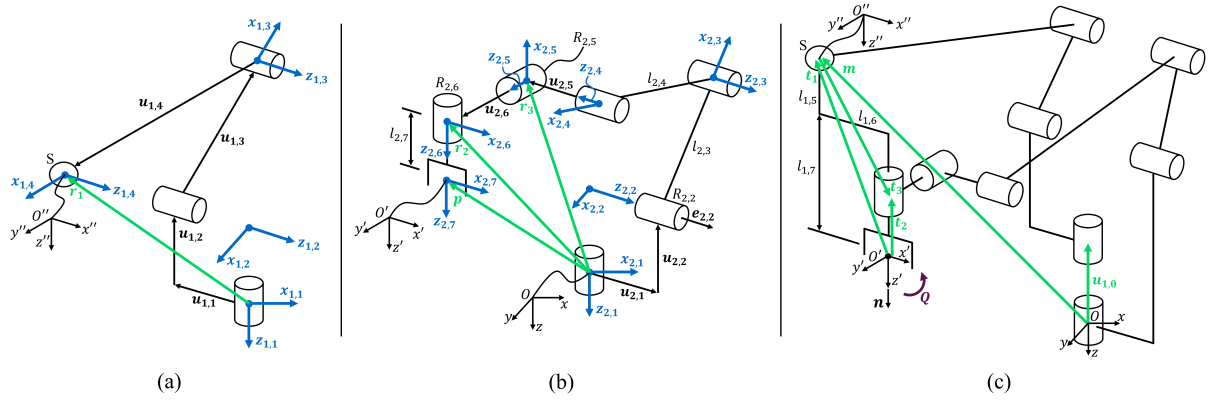

(a) (b) (c)

Fig. 2. Geometric description of the proposed 6-DOF hybrid parallel robot: a) leg 1, b) leg 2, and c) complete robot.

the same form as (3), now expressed in terms of $\theta_{1,2}$. The corresponding coefficients are

$$\begin{aligned} A &= -2l_{1,3}\left(l_{1,2}+r_{1,z}\right), \\ B &= -2l_{1,3}\left(r_{1,x}\mathrm{c}_{1,1}+r_{1,y}\mathrm{s}_{1,1}\right), \\ C &= 2l_{1,1}r_{1,x}\mathrm{s}_{1,1}-2l_{1,1}r_{1,y}\mathrm{c}_{1,1}+2l_{1,2}r_{1,z} \\ &\quad +l_{1,1}^2+l_{1,2}^2+l_{1,3}^2-l_{1,4}^2+r_{1,x}^2+r_{1,y}^2+r_{1,z}^2, \end{aligned}$$

where $r_{1,z}$ is the third component of $\mathbf{r}_1$. This equation can then be solved for $\theta_{1,2}$ using the same approach as for (3).

Then, to solve for $\theta_{1,3}$, the first step is to isolate $\mathrm{c}_{1,23}$ from either the first or second row of $\mathbf{r}_1$ and $\mathrm{s}_{1,23}$ from the third row of $\mathbf{r}_1$. Angle $\theta_{1,3}$ can then be calculated as

$$\theta_{1,3} = \mathrm{atan2}(\mathrm{s}_{1,23},\, \mathrm{c}_{1,23}) - \theta_{1,2}. \tag{4}$$

The above analysis demonstrates that the inverse kinematics of leg 1 has at most four solutions.

B. Leg 2

To solve the inverse kinematics of leg 2, the position vector of joint $R_{2,6}$ is first calculated with

$$\mathbf{r}_2 = \mathbf{p} + \mathbf{Q}\mathbf{t}_2. \tag{5}$$

The forward kinematics for the position of joint $R_{2,6}$ then yields

$$\mathbf{r}_2 = \mathbf{a}_{2,1} + \mathbf{Q}_{2,1}\Big(\mathbf{a}_{2,2} + \mathbf{Q}_{2,2}\Big(\mathbf{a}_{2,3} + \mathbf{Q}_{2,3}\big(\mathbf{a}_{2,4} + \mathbf{Q}_{2,4}\mathbf{a}_{2,5}\big)\Big)\Big). \tag{6}$$

A linear combination of the first two rows of (6), weighted by $\mathrm{s}_{2,1}$ and $\mathrm{c}_{2,1}$, yields

$$r_{2,x}\mathrm{s}_{2,1} - r_{2,y}\mathrm{c}_{2,1} - l_{2,1} + l_{2,5} = 0, \tag{7}$$

which is of the same form as (3). Consequently, $\theta_{2,1}$ can be solved in the same way using the half-angle substitution.

Then, to solve for $\theta_{2,5}$ and $\theta_{2,6}$, the rotation matrix describing the orientation of the end-effector relative to the base frame is considered,

$$\mathbf{Q} = \mathbf{Q}_{2,1}\mathbf{Q}_{2,2}\mathbf{Q}_{2,3}\mathbf{Q}_{2,4}\mathbf{Q}_{2,5}\mathbf{Q}_{2,6}\,. \tag{8}$$

By exploiting the orthogonality of rotation matrices and using the known value of $\mathbf{Q}_{2,1}$, it follows that

$$\mathbf{Q}^{\mathrm{T}}\mathbf{Q}_{2,1} = \mathbf{Q}_{2,6}^{\mathrm{T}}\mathbf{Q}_{2,5}^{\mathrm{T}}\mathbf{Q}_{2,4}^{\mathrm{T}}\mathbf{Q}_{2,3}^{\mathrm{T}}\mathbf{Q}_{2,2}^{\mathrm{T}}. \tag{9}$$

Here, $\mathbf{Q}^{\mathrm{T}}\mathbf{Q}_{2,1}$ can be directly calculated while the right-most part of (9) expands explicitly to

$$\mathbf{Q}_{2,6}^{\mathrm{T}}\mathbf{Q}_{2,5}^{\mathrm{T}}\mathbf{Q}_{2,4}^{\mathrm{T}}\mathbf{Q}_{2,3}^{\mathrm{T}}\mathbf{Q}_{2,2}^{\mathrm{T}} = \begin{bmatrix} \bullet & \bullet & -\mathrm{s}_{2,5}\mathrm{c}_{2,6} \\ \bullet & \bullet & \mathrm{s}_{2,5}\mathrm{s}_{2,6} \\ \bullet & \bullet & \mathrm{c}_{2,5} \end{bmatrix}, \tag{10}$$

where the entries denoted by $\bullet$ are not required for the inverse kinematics. To solve for $\theta_{2,5}$, the inverse cosine of the last component is computed, yielding two solutions for $\theta_{2,5}$. Once $\theta_{2,5}$ is determined, $\theta_{2,6}$ can be readily obtained from the remaining components of (10), namely by computing $\mathrm{c}_{2,6}$ and $\mathrm{s}_{2,6}$. This approach is valid provided $\mathrm{s}_{2,5} \neq 0$, which corresponds to a singular configuration that is discussed later and will be avoided during operation.

With $\theta_{2,5}$ and $\theta_{2,6}$ known, the position of joint $R_{2,5}$ relative to the base frame can be computed with

$$\mathbf{r}_3 = \mathbf{p} + \mathbf{Q}\left(\mathbf{t}_2 - \mathbf{Q}_{2,6}^{\mathrm{T}}\mathbf{Q}_{2,5}^{\mathrm{T}}\mathbf{u}_{2,6}\right), \tag{11}$$

where $\mathbf{u}_{2,6} = \begin{bmatrix} 0 & 0 & l_{2,6} \end{bmatrix}^{\mathrm{T}}$ is expressed in frame $(2,5)$. The forward kinematics for the position of joint $R_{2,5}$ yields

$$\mathbf{r}_3 = \mathbf{a}_{2,1} + \mathbf{Q}_{2,1}\left(\mathbf{a}_{2,2} + \mathbf{Q}_{2,2}\left(\mathbf{a}_{2,3} + \mathbf{Q}_{2,3}\mathbf{a}_{2,4}\right)\right). \tag{12}$$

Rearranging all three rows of (12) and taking the sum of squares of these rows leads to an equation of the same form as (3) expressed in terms of $\theta_{2,2}$, in which all coefficients are known expressions. The value of $\theta_{2,2}$ is then obtained using the same half-angle substitution method as for (3).

Next, to solve for $\theta_{2,3}$, the first step is to isolate $\mathrm{c}_{2,23}$ from either the first or second row of (12) and $\mathrm{s}_{2,23}$ from the third row of (12). Angle $\theta_{2,3}$ is then computed as

$$\theta_{2,3} = \mathrm{atan2}(\mathrm{s}_{2,23},\, \mathrm{c}_{2,23}) - \theta_{2,2}. \tag{13}$$

Finally, $\theta_{2,4}$ is determined from the rotation matrix $\mathbf{Q}_{2,4}$, given by

$$\mathbf{Q}_{2,4} = \begin{bmatrix} \mathrm{c}_{2,4} & 0 & \mathrm{s}_{2,4} \\ \mathrm{s}_{2,4} & 0 & -\mathrm{c}_{2,4} \\ 0 & 1 & 0 \end{bmatrix}. \tag{14}$$

Using the known values of the other joint angles, $\mathbf{Q}_{2,4}$ can be computed with

$$\mathbf{Q}_{2,4} = \mathbf{Q}_{2,3}^{\mathrm{T}}\mathbf{Q}_{2,2}^{\mathrm{T}}\mathbf{Q}_{2,1}^{\mathrm{T}}\mathbf{Q}\mathbf{Q}_{2,6}^{\mathrm{T}}\mathbf{Q}_{2,5}^{\mathrm{T}}. \tag{15}$$

Angle $\theta_{2,4}$ is obtained from the first two rows of the first column of (14) as

$$\theta_{2,4} = \text{atan2}(\text{s}_{2,4},\, \text{c}_{2,4}). \tag{16}$$

Thus, the inverse kinematics of leg 2 has at most eight solutions. Consequently, considering both legs, the CoPaRo architecture has at most 32 inverse kinematics solutions.

IV. Forward Kinematics

The forward kinematics consists in determining the position and orientation of the end-effector from the actuated joint angles. The forward kinematics of each leg developed in Section III is reused here. In particular, the position of joint $R_{2,5}$, noted $\mathbf{r}_3$, is obtained from (12), and the position $\mathbf{r}_1$ is obtained from (2). The position of the spherical joint relative to the base frame is then expressed as

$$\mathbf{m} = \mathbf{r}_1 + \mathbf{u}_{1,0}. \tag{17}$$

The position of $\mathbf{r}_2$ is determined geometrically. Specifically, $\mathbf{r}_2$ corresponds to the intersection between a sphere of radius $\sqrt{l_{1,6}^2 + (l_{1,5} + l_{1,7} - l_{2,7})^2}$, centered at the spherical joint, and a circle of radius $l_{2,6}$ centered at $\mathbf{r}_3$ with normal vector $\mathbf{e}_{2,2}$. This intersection yields two possible solutions for $\mathbf{r}_2$. The vector from $\mathbf{r}_3$ to $\mathbf{r}_2$ in the base reference frame is defined as

$$\mathbf{v} = \mathbf{r}_2 - \mathbf{r}_3, \tag{18}$$

and axis z' is constrained to be orthogonal to $\mathbf{v}$, which yields

$$\mathbf{v}^{\mathrm{T}}\mathbf{e}_{z'} = 0, \tag{19}$$

where $\mathbf{e}_{z'}$ is the unit vector along axis z' expressed in the base frame. The vector from the centre of revolute joint $R_{2,6}$ to the centre of the spherical joint is defined as

$$\mathbf{b} = \mathbf{m} - \mathbf{r}_2. \tag{20}$$

Its projection onto axis z' must satisfy

$$\mathbf{b}^{\mathrm{T}}\mathbf{e}_{z'} = -l_{1,5} - l_{1,7} + l_{2,7}, \tag{21}$$

which imposes a conical constraint. The unit-length requirement

$$\|\mathbf{e}_{z'}\| = 1 \tag{22}$$

defines a spherical constraint. The intersection of the spherical constraint (22), the plane defined by the orthogonality condition (19), and the conical constraint (21) yields two possible solutions for $\mathbf{e}_{z'}$. Given $\mathbf{e}_{z'}$, the unit vector along axis y' in the base frame is defined by

$$\mathbf{e}_{y'} = \frac{\mathbf{b} \times \mathbf{e}_{z'}}{\|\mathbf{b} \times \mathbf{e}_{z'}\|}, \tag{23}$$

and the unit vector along axis x' directly follows, thereby completing a right-handed orthonormal basis. The orientation of the platform relative to the base frame is expressed by

$$\mathbf{Q} = \begin{bmatrix} \mathbf{e}_{x'} & \mathbf{e}_{y'} & \mathbf{e}_{z'} \end{bmatrix}, \tag{24}$$

and the position of the end-effector is given by

$$\mathbf{p} = \mathbf{r}_2 + l_{2,7}\mathbf{e}_{z'}. \tag{25}$$

Globally, the forward kinematics of the CoPaRo architecture admits up to four solutions.

V. Velocity equations

The Jacobians derived from the velocity equations enable the identification of all singularity conditions of the architecture. To simplify the singularity analysis, the velocity equations are expressed with respect to frame $O''_{x''y''z''}$, which is attached to the end-effector and has its origin at the centre of the spherical joint. As mentioned previously, frame $O''_{x''y''z''}$ is always aligned with frame $O'_{x'y'z'}$, differing only in position.

The first three constraints are obtained from the position of the spherical joint with respect to the base frame, as given in (17). Differentiating (17) yields the first three velocity equations, given by

$$\dot{\mathbf{m}} = \dot{\mathbf{r}}_1 = \mathbf{M}_1\dot{\boldsymbol{\theta}}_1, \tag{26}$$

where $\dot{\boldsymbol{\theta}}_1 = \begin{bmatrix} \dot{\theta}_{1,1} & \dot{\theta}_{1,2} & \dot{\theta}_{1,3} \end{bmatrix}^{\mathrm{T}}$ and $\mathbf{M}_1$ denotes the Jacobian matrix of leg 1.

The fourth constraint is imposed on the length of the sixth link of leg 2, expressed as

$$\mathbf{v}^{\mathrm{T}}\mathbf{v} = l_{2,6}^2, \tag{27}$$

where $\mathbf{v}$ is defined in (18). Differentiating (27) results in

$$\mathbf{v}^{\mathrm{T}}\dot{\mathbf{v}} = 0. \tag{28}$$

Considering

$$\mathbf{r}_2 = \mathbf{m} + \mathbf{Q}\mathbf{t}_3, \tag{29}$$

the time derivative of $\mathbf{v}$ is obtained by differentiating (12) and (29),

$$\dot{\mathbf{v}} = \dot{\mathbf{r}}_2 - \dot{\mathbf{r}}_3 = \dot{\mathbf{m}} + \boldsymbol{\omega} \times (\mathbf{Q}\mathbf{t}_3) - \mathbf{M}_2\dot{\boldsymbol{\theta}}_2, \tag{30}$$

where $\dot{\boldsymbol{\theta}}_2 = \begin{bmatrix} \dot{\theta}_{2,1} & \dot{\theta}_{2,2} & \dot{\theta}_{2,3} \end{bmatrix}^{\mathrm{T}}$, $\boldsymbol{\omega}$ denotes the angular velocity of the end-effector, and $\mathbf{M}_2$ is the positioning Jacobian associated with the first four degrees of freedom of leg 2, defined from the base to $\mathbf{r}_3$. Substitution of (30) into (28) results in

$$\mathbf{v}^{\mathrm{T}}\dot{\mathbf{m}} + \mathbf{v}^{\mathrm{T}}(\boldsymbol{\omega} \times \mathbf{Q}\mathbf{t}_3) - \mathbf{v}^{\mathrm{T}}\mathbf{M}_2\dot{\boldsymbol{\theta}}_2 = 0. \tag{31}$$

Applying the scalar triple product identity

$$\mathbf{a}^{\mathrm{T}}(\mathbf{b} \times \mathbf{c}) = (\mathbf{c} \times \mathbf{a})^{\mathrm{T}}\mathbf{b}$$

transforms this expression into

$$\mathbf{v}^{\mathrm{T}}\dot{\mathbf{m}} + (\mathbf{Q}\mathbf{t}_3 \times \mathbf{v})^{\mathrm{T}}\boldsymbol{\omega} = \mathbf{v}^{\mathrm{T}}\mathbf{M}_2\dot{\boldsymbol{\theta}}_2, \tag{32}$$

representing the fourth velocity equation.

The fifth constraint enforces orthogonality between the unit vector normal to the end-effector $\mathbf{n}$, and vector $\mathbf{v}$, expressed as

$$\mathbf{n}^{\mathrm{T}}\mathbf{v} = 0. \tag{33}$$

Differentiation of this constraint results in

$$\mathbf{v}^{\mathrm{T}}\dot{\mathbf{n}} + \mathbf{n}^{\mathrm{T}}\dot{\mathbf{v}} = 0. \tag{34}$$

Substituting (30) for $\dot{\mathbf{v}}$ and expressing the time derivative of $\mathbf{n}$ as $\dot{\mathbf{n}} = \boldsymbol{\omega} \times \mathbf{n}$ leads to

$$(\mathbf{n} \times \mathbf{v})^{\mathrm{T}}\boldsymbol{\omega} + \mathbf{n}^{\mathrm{T}}\dot{\mathbf{m}} + ((\mathbf{Q}\mathbf{t}_3) \times \mathbf{n})^{\mathrm{T}}\boldsymbol{\omega} - \mathbf{n}^{\mathrm{T}}\mathbf{M}_2\dot{\boldsymbol{\theta}}_2 = 0. \tag{35}$$

Using the linearity of the cross product, this expression simplifies to

$$\mathbf{n}^{\mathrm{T}}\dot{\mathbf{m}} + (\mathbf{n} \times (\mathbf{v} - \mathbf{Q}\mathbf{t}_3))^{\mathrm{T}}\boldsymbol{\omega} = \mathbf{n}^{\mathrm{T}}\mathbf{M}_2\dot{\boldsymbol{\theta}}_2, \tag{36}$$

representing the fifth velocity equation.

The sixth constraint enforces orthogonality between the axis of joint $R_{2,2}$ and the axis of joint $R_{2,5}$. A unit vector $\mathbf{e}_{2,2} = \begin{bmatrix}\sin(\theta_{2,1}) & -\cos(\theta_{2,1}) & 0\end{bmatrix}^{\mathrm{T}}$ is defined along the axis of joint $R_{2,2}$, while $\mathbf{v}$ lies in the direction of the axis of joint $R_{2,5}$. This constraint is written as

$$\mathbf{e}_{2,2}^{\mathrm{T}}\mathbf{v} = 0. \tag{37}$$

Differentiation of the constraint results in

$$\mathbf{v}^{\mathrm{T}}\dot{\mathbf{e}}_{2,2} + \mathbf{e}_{2,2}^{\mathrm{T}}\dot{\mathbf{v}} = 0. \tag{38}$$

Substituting (30) for $\dot{\mathbf{v}}$ and expressing the derivative of $\mathbf{e}_{2,2}$ as $\dot{\mathbf{e}}_{2,2} = \mathbf{M}_3\dot{\boldsymbol{\theta}}_2$, with

$$\mathbf{M}_3 = \begin{bmatrix}\cos\theta_{2,1} & 0 & 0\\ \sin\theta_{2,1} & 0 & 0\\ 0 & 0 & 0\end{bmatrix},$$

leads to

$$\mathbf{e}_{2,2}^{\mathrm{T}}\dot{\mathbf{m}} + \big((\mathbf{Q}\mathbf{t}_3)\times\mathbf{e}_{2,2}\big)^{\mathrm{T}}\boldsymbol{\omega} = \big(\mathbf{e}_{2,2}^{\mathrm{T}}\mathbf{M}_2 - \mathbf{v}^{\mathrm{T}}\mathbf{M}_3\big)\dot{\boldsymbol{\theta}}_2. \tag{39}$$

This expression represents the sixth velocity equation.

Collecting the velocity equations (26), (32), (36), and (39) finally yields the global velocity equations of the robot, written as

$$\mathbf{K}\begin{bmatrix}\dot{\boldsymbol{\theta}}_1\\ \dot{\boldsymbol{\theta}}_2\end{bmatrix} = \mathbf{J}\begin{bmatrix}\dot{\mathbf{m}}\\ \boldsymbol{\omega}\end{bmatrix}, \tag{40}$$

with

$$\mathbf{K} = \begin{bmatrix}\mathbf{M}_1 & \mathbf{0}_{3\times3}\\ \mathbf{0}_{1\times3} & \mathbf{v}^{\mathrm{T}}\mathbf{M}_2\\ \mathbf{0}_{1\times3} & \mathbf{n}^{\mathrm{T}}\mathbf{M}_2\\ \mathbf{0}_{1\times3} & \mathbf{e}_{2,2}^{\mathrm{T}}\mathbf{M}_2 - \mathbf{v}^{\mathrm{T}}\mathbf{M}_3\end{bmatrix}, \tag{41}$$

$$\mathbf{J} = \begin{bmatrix}\mathbf{I}_{3\times3} & \mathbf{0}_{3\times3}\\ \mathbf{v}^{\mathrm{T}} & ((\mathbf{Q}\mathbf{t}_3)\times\mathbf{v})^{\mathrm{T}}\\ \mathbf{n}^{\mathrm{T}} & (\mathbf{n}\times(\mathbf{v}-\mathbf{Q}\mathbf{t}_3))^{\mathrm{T}}\\ \mathbf{e}_{2,2}^{\mathrm{T}} & ((\mathbf{Q}\mathbf{t}_3)\times\mathbf{e}_{2,2})^{\mathrm{T}}\end{bmatrix}. \tag{42}$$

VI. Singularity Analysis

The singularity analysis will determine the limitations of the CoPaRo architecture in terms of reachable workspace because the robot loses controllability in singular configurations due to the Jacobian losing rank.

Due to the block-diagonal structure of $\mathbf{K}$, its determinant factorizes as

$$\det(\mathbf{K}) = \det\left(\begin{bmatrix}\mathbf{K}_{11} & \mathbf{0}_{3\times3}\\ \mathbf{0}_{3\times3} & \mathbf{K}_{22}\end{bmatrix}\right) = \det(\mathbf{K}_{11})\det(\mathbf{K}_{22}), \tag{43}$$

where

$$\mathbf{K}_{11} = \mathbf{M}_1, \qquad \mathbf{K}_{22} = \begin{bmatrix}\mathbf{v}^{\mathrm{T}}\mathbf{M}_2\\ \mathbf{n}^{\mathrm{T}}\mathbf{M}_2\\ \mathbf{e}_{2,2}^{\mathrm{T}}\mathbf{M}_2 - \mathbf{v}^{\mathrm{T}}\mathbf{M}_3\end{bmatrix}.$$

Therefore, $\mathbf{K}$ is singular whenever $\det(\mathbf{K}_{11}) = 0$ or $\det(\mathbf{K}_{22}) = 0$. This result is consistent with the structure of the mechanism, which consists of two serial chains connected by the platform that closes the kinematic loop. Thus, type I singularities can be identified independently for each serial chain. The determinant of $\mathbf{K}_{11}$ can be written as

$$\det(\mathbf{K}_{11}) = -l_{1,3}l_{1,4}\mathrm{s}_{1,3}\Big(l_{1,3}\mathrm{c}_{1,2} + l_{1,4}\mathrm{c}_{1,23}\Big). \tag{44}$$

From (44), four singularity conditions arise for the first serial chain (leg 1), namely, 1.1) $l_{1,3} = 0$, 1.2) $l_{1,4} = 0$, 1.3) $\mathrm{s}_{1,3} = 0$, 1.4) $l_{1,3}\mathrm{c}_{1,2} + l_{1,4}\mathrm{c}_{1,23} = 0$. Conditions 1.1 and 1.2 effectively eliminate one degree of freedom in leg 1 by overlapping joints. Condition 1.3 corresponds to segments $\mathbf{u}_{1,3}$ and $\mathbf{u}_{1,4}$ being parallel, which prevents motion of the spherical joint in the direction parallel to these segments, thereby removing one degree of freedom. Condition 1.4 occurs when the spherical joint lies in the plane spanned by segments $\mathbf{u}_{1,1}$ and $\mathbf{u}_{1,2}$, which prevents motion of the spherical joint in the direction parallel to $\mathbf{u}_{1,1}$ and again removes one degree of freedom.

For the second serial chain (leg 2), the determinant of $\mathbf{K}_{22}$ can be written as

$$\det(\mathbf{K}_{22}) = l_{2,3}l_{2,4}l_{2,6}\mathrm{s}_{2,3}\mathrm{s}_{2,5}\Big(l_{2,3}\mathrm{c}_{2,2} + l_{2,4}\mathrm{c}_{2,23} - l_{2,6}\mathrm{s}_{2,234}\Big). \tag{45}$$

This leads to six singularity conditions for leg 2, namely, 2.1) $l_{2,3} = 0$, 2.2) $l_{2,4} = 0$, 2.3) $l_{2,6} = 0$, 2.4) $\mathrm{s}_{2,3} = 0$, 2.5) $\mathrm{s}_{2,5} = 0$, 2.6) $l_{2,3}\mathrm{c}_{2,2} + l_{2,4}\mathrm{c}_{2,23} - l_{2,6}\mathrm{s}_{2,234} = 0$. Conditions 2.1, 2.2, and 2.4 are equivalent to conditions 1.1, 1.2, and 1.3 of leg 1, respectively. Condition 2.3 corresponds to a type III singularity and will be discussed in more detail later. Condition 2.5 arises when $\mathbf{u}_{2,5}$ and $\mathbf{n}$ are parallel, which removes one rotational degree of freedom at the platform. Condition 2.6 occurs when joint $R_{2,6}$ lies in the plane spanned by segments $\mathbf{u}_{2,1}$ and $\mathbf{u}_{2,2}$, which prevents motion of joint $R_{2,6}$ in the direction parallel to $\mathbf{u}_{2,1}$ and thereby removes one degree of freedom at the platform.

Next, the following analysis addresses the moving platform singularities (type II), which represent the most restrictive cases in parallel architectures. These singularities occur within the workspace and often impose limitations on the achievable orientations. Mathematically, they are characterized by the condition $\det(\mathbf{J}) = 0$, where $\mathbf{J}$ denotes the Jacobian matrix from (42). Since $\mathbf{J}$ has a block lower triangular structure, its determinant can be expressed as

$$\det(\mathbf{J}) = \det(\mathbf{I}_{3\times3})\det\left(\begin{bmatrix}((\mathbf{Q}\mathbf{t}_3)\times\mathbf{v})^{\mathrm{T}}\\ (\mathbf{n}\times(\mathbf{v}-\mathbf{Q}\mathbf{t}_3))^{\mathrm{T}}\\ ((\mathbf{Q}\mathbf{t}_3)\times\mathbf{e}_{2,2})^{\mathrm{T}}\end{bmatrix}\right) \tag{46}$$

$$\det(\mathbf{J}) = l_{1,6}l_{2,6}^2\mathrm{c}_{2,6}\Big((l_{1,5} + l_{1,7} - l_{2,7})\,\mathrm{s}_{2,5} + l_{1,6}\mathrm{c}_{2,5}\mathrm{c}_{2,6}\Big). \tag{47}$$

Accordingly, the four parallel singularity conditions are 3.1) $l_{1,6} = 0$, 3.2) $l_{2,6} = 0$, 3.3) $\mathrm{c}_{2,6} = 0$, 3.4) $(l_{1,5} + l_{1,7} - l_{2,7})\,\mathrm{s}_{2,5} + l_{1,6}\mathrm{c}_{2,5}\mathrm{c}_{2,6} = 0$. To better understand these singularity conditions, a geometric interpretation is provided. Each of the six rows in $\mathbf{J}$ can be represented as a line using Plücker coordinates, as illustrated

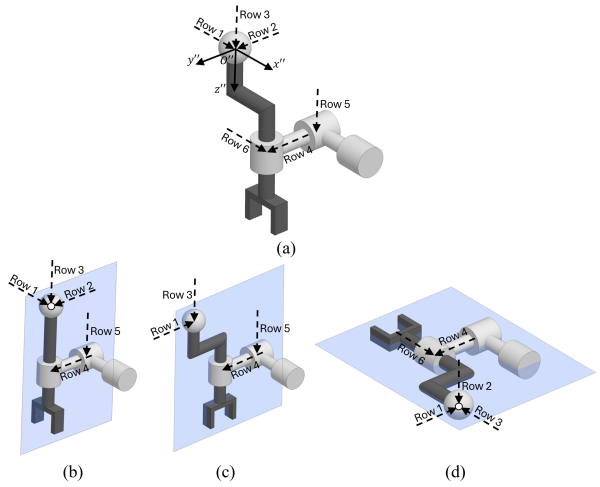

Fig. 3. (a) Plücker line representation of the six rows of the Jacobian $\mathbf{J}$. The geometric configurations of platform singularity conditions (b) 3.1, (c) 3.3, and (d) 3.4 are shown for the 6-DOF hybrid parallel robot.

in Fig. 3(a). Using Grassmann line geometry (GLG), it is possible to determine geometrically the conditions under which these lines (the Jacobian rows) become linearly dependent, corresponding to the singularities of $\mathbf{J}$ identified above. Further details on the application of GLG to parallel manipulators can be found in [14]. Singularity condition 3.1 occurs when Plücker lines 1 through 5 become linearly dependent, causing the associated linear system to degenerate to rank 4, corresponding to case 4d of GLG. In this configuration, lines 1, 2, and 3 intersect at a point lying on the plane spanned by lines 4 and 5, as shown in Fig. 3(b). Condition 3.2 (also condition 2.3) represents a type III singularity, in which both $\mathbf{K}$ and $\mathbf{J}$ are singular due to the fourth row of each matrix becoming $\mathbf{0}_{1\times 6}$. This singularity arises because the platform effectively reduces to two spherical joints connected by a rigid link, allowing an uncontrollable rotation about the line passing through both joints. Condition 3.3 corresponds to case 3d of GLG, in which lines 1, 3, 4, and 5 lie in a common plane, as illustrated in Fig. 3(c), causing the corresponding linear system to degenerate to rank 3. Condition 3.4 arises when the spherical joint lies in the plane defined by lines 4 and 6. Equivalently, lines 1, 2, and 3 intersect at a point on this plane, causing the corresponding linear system to degenerate to rank 4, according to case 4d of GLG, as shown in Fig. 3(d).

This concludes the singularity analysis for the proposed hybrid parallel architecture. To summarize, the conditions labeled 1.x and 2.x correspond to type I singularities, while the conditions 3.x represent type II singularities, except for condition 2.3/3.2, which is a type III singularity. The rank-based interpretations provided above clarify how each condition reflects a degeneracy of the linear system associated with the Jacobian, linking the algebraic singularity to its geometric manifestation.

The orientation of the end-effector is described using tilt and torsion angles $(\phi, \theta_{tt}, \sigma)$ [15], where ϕ denotes the azimuth, θ_{tt} the tilt angle, and σ the torsion angle. Considering the singularity conditions described above, in the zero-torsion case, the rotation of the end-effector is constrained to a maximum tilt of $\theta_{tt} = 90^\circ$ for $\phi = 0^\circ$ and $\phi = 180^\circ$, as imposed by type I singularity condition 2.5 and type II singularity condition 3.4. This limit increases as ϕ approaches $\pm 90^\circ$, where no singularity constraints are present and the tilt angle can reach unbounded values, allowing infinite rotation of the platform. The torsion angle of the end-effector is constrained to $\sigma = \pm 90^\circ$ by singularity condition 3.3, thereby defining the torsional limits of the workspace. Therefore, considering only the singularity conditions, the orientational workspace of the CoPaRo architecture is characterized by a torsion angle ranging from $\sigma = -90^\circ$ to $\sigma = 90^\circ$, and a zero-torsion tilt angle ranging from a maximum of $\theta_{tt} = 90^\circ$ in its most constrained direction to $\theta_{tt} = 180^\circ$ (infinite rotation) in its least constrained direction.

VII. Workspace Analysis

To determine both the translational and orientational workspace, a numerical approach is employed. For each position and orientation under consideration, the inverse kinematics is computed to verify the existence of a feasible solution within the same solution branch among the 32 possible branches. Additionally, the condition number of the Jacobian matrices $\mathbf{K}$ and $\mathbf{J}$ is evaluated, and configurations are considered ill-conditioned if the condition number of either matrix exceeds 80*. This threshold ensures avoidance of configurations with high kinematic sensitivity or poor numerical stability, while a finite condition number guarantees that the corresponding Jacobian is full rank, indicating that the robot is not in a singular configuration. In addition, potential interferences between links are evaluated for each configuration. To assess collisions between non-adjacent links, the links are modeled as line segments, and the minimum distance between each pair is computed. If this distance is less than 20 mm, the configuration is considered to have an interference and is excluded from the workspace. Consequently, the workspace obtained in this section corresponds to configurations that are well-conditioned, free of singularities, and free of interferences, thereby providing a realistic representation of the robot's usable workspace. The lengths of the links can be proportionally increased or decreased to expand or reduce the translational workspace accordingly. Such scaling does not affect the orientational workspace, provided that no new interferences between links are introduced. The geometric parameters for the workspace analysis were selected as follows (all values in millimeters):

$$l_{1,0} = 80,\ l_{1,1} = l_{2,1} = 82.16,\ l_{1,2} = 104.43,\ l_{1,3} = 645.42,$$
$$l_{1,4} = 567.55,\ l_{1,5} = 55.31,\ l_{1,6} = 39.76,\ l_{1,7} = 117.30,\ l_{2,2} = 126.89,$$
$$l_{2,3} = 510,\ l_{2,4} = 588.08,\ l_{2,5} = 147.58,\ l_{2,6} = 98.86,\ l_{2,7} = 37.98.$$

These values were determined through a Pareto optimization aimed at maximizing both the translational and orientational workspace of the robot.

*As the workspace showed only minor variation for maximum condition numbers between 60 and 100, the mid-range value of 80 was selected to balance ill-conditioning and workspace size.

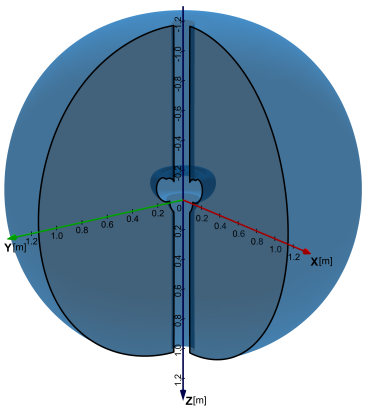

Fig. 4. Translational workspace of the CoPaRo architecture, with axes corresponding to the base frame O_{xyz}.

A. Translational Workspace

To construct the translational workspace of the robot, the platform is oriented at $\mathbf{Q} = \mathbf{I}_{3\times3}$, representing the reference orientation in which frame $O'_{x'y'z'}$ remains aligned with the base frame O_{xyz}. In this configuration, the platform's y'-axis is orthogonal and points away from the first two coaxial revolute joints for values of $x = 0$. Since the first revolute joint of each leg is coaxial, the translational workspace is symmetric around their common axis. Therefore, the workspace can first be determined in the y-z plane, and the resulting 2D workspace can then be revolved around this axis to generate the complete 3D translational workspace. The 2D workspace is discretized using a grid with 0.5 mm intervals, providing a smooth resolution for visualization. The resulting 3D translational workspace is shown in Fig. 4, with axes corresponding to the base frame O_{xyz}, which is located at the centre of the first revolute joint of leg 2. A section of the revolution is left open to allow visualization of the complete translational workspace. The CoPaRo architecture possesses a translational workspace resembling that of a serial robot, forming an approximately spherical volume centered at the robot's base, which represents an ideal workspace shape.

B. Orientational Workspace

The orientational workspace was evaluated at an end-effector position $\mathbf{p}$ corresponding to the centroid of the negative-z, positive-y portion of the 2D translational workspace slice at $x = 0$, which was used previously to construct the full 3D translational workspace via revolution. This position is representative of the region around which the robot is expected to operate most frequently. Due to the rotational symmetry around the common axis of the first revolute joint of each leg, the orientational workspace obtained at point $\mathbf{p}$ can be applied to all positions generated by revolving $\mathbf{p}$ around this axis. Tilt and torsion angles, as previously introduced, are used to describe the platform orientation. For the numerical construction of the orientational workspace, the tilt and torsion angles are discretized with intervals of 1° for σ, and 0.1° for both θ_{tt} and ϕ. This fine discretization ensures an accurate representation

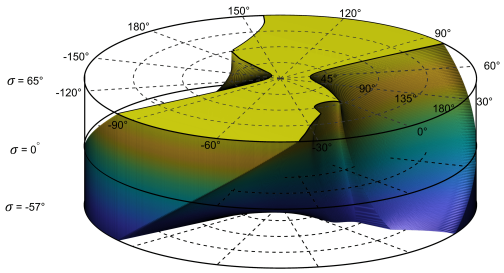

Fig. 5. Orientational workspace of the CoPaRo architecture at the reference position, defined as the centroid of the negative-z, positive-y portion of the 2D translational workspace slice at $x = 0$. Coloring is arbitrary and used solely for visual clarity.

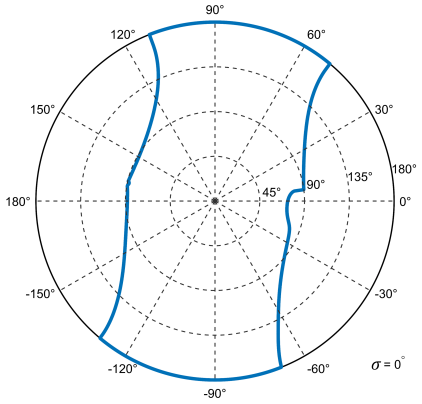

Fig. 6. Largest tilt angles in the zero-torsion cross-section of the proposed architecture's orientational workspace.

of the workspace boundaries and smooth visualization. The resulting workspace of the CoPaRo architecture is illustrated in Fig. 5 using cylindrical coordinates, where the z-axis, radius, and azimuthal angle correspond to σ, θ_{tt}, and ϕ, respectively. The CoPaRo architecture allows for a range of torsion angles, extending from $\sigma = -57^\circ$ to $\sigma = 65^\circ$. It can be observed that the tilt angle becomes limited at larger torsion angles, but remains generally very large. The zero-torsion cross-section of the orientational workspace is shown in Fig. 6. In the zero-torsion case, the platform can reach tilt angles close to 90° in all directions and can achieve infinite rotation in certain directions. This behavior is consistent with the predictions presented in Section VI, confirming that the zero-torsion workspace is limited by the singularities of the architecture. It should be noted, however, that not all boundaries correspond to singular configurations; some are caused by interferences between links or by ill-conditioned Jacobian matrices. For instance, the range of torsion is restricted by ill-conditioned Jacobians rather than singularities, which explains why the full theoretical range of $\sigma = \pm 90^\circ$ discussed in Section VI is not attained in practice. Despite these limitations, the platform exhibits excellent rotational capabilities, considering that the computed workspace represents the usable orientational workspace, accounting for singularities, interferences, and numerical stability. In fact, the orientational capabilities observed at the centroid position are maintained throughout most of the translational

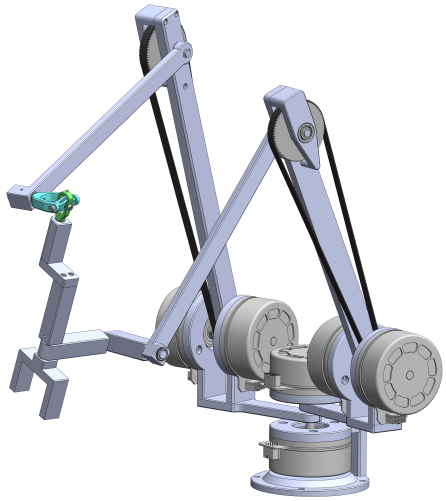

Fig. 7. CAD model of the CoPaRo robot.

workspace. Therefore, the dextrous workspace is defined here as the region in which the manipulator preserves the same orientational capabilities as those evaluated at the workspace centroid. The volume of this dextrous workspace closely approximates the translational workspace depicted in Fig. 4; however, the orientational capability typically decreases significantly within 0.1 m of the translational boundaries.

VIII. Virtual Prototype

A CAD model of a generic embodiment of the novel CoPaRo architecture is shown in Fig. 7. A 4-DoF spherical joint [16] is employed to provide a large motion range. As shown in Fig. 7, the motors are positioned close to the base and transmit motion to distal joints via pulleys. This arrangement significantly reduces the robot's inertia, as the motors are the heaviest components. The low inertia allows the use of direct-drive or quasi-direct-drive motors, which render the robot backdrivable. The required transmission ratio lies in the range 3:1–5:1, compared to values typically exceeding 50:1 in serial manipulators. As reflected inertia scales with the square of the reduction ratio, this significantly reduces the apparent joint inertia. The use of timing belt reduction lowers friction relative to high-ratio planetary, harmonic, or cycloidal gear drives, thereby further enhancing backdrivability. Backdrivability is advantageous for human-robot interaction, as it allows the robot to react smoothly to forces applied by a human, enabling more intuitive and fluid interaction while sensing the forces directly through the actuators instead of relying on additional force/torque sensors, also referred to as proprioceptive actuation [17]. Despite placing the motors near the base, the robot maintains a compact footprint comparable to that of serial manipulators. An animation of the robot is provided as supplemental material, demonstrating both the translational and rotational motion of the platform and highlighting its large workspace.

IX. Conclusion

This paper introduced CoPaRo, a novel 6-DOF hybrid parallel robot. Its complete kinematic analysis was presented, and all singular configurations were analyzed. The proposed architecture achieves a large usable translational and orientational workspace, accounting for singularities, mechanical interferences, and numerical stability. The axisymmetric translational workspace closely resembles that of a serial robot, which is ideal. The orientational workspace provides infinite rotation in certain directions and close to 90° in all directions under zero torsion, with platform torsion ranging from -57° to 65°. A virtual prototype shows that the actuators can be positioned close to the base, transmitting motion to distal links via pulleys to reduce the robot's inertia. The low inertia also allows the use of direct-drive or quasi-direct-drive actuators, enabling backdrivability. These characteristics make CoPaRo highly suitable for pHRI tasks. Future work will focus on the development of a functional prototype and its validation in pHRI tasks.

References

[1] A. Cherubini et al., "Collaborative manufacturing with physical human–robot interaction," *Robotics and Computer-Integrated Manufacturing*, vol. 40, pp. 1–13, 2016.

[2] A. Q. Keemink et al., "Admittance control for physical human–robot interaction," *Int. J. Robot. Res.*, vol. 37, no. 11, pp. 1421–1444, 2018.

[3] D. V. Gealy et al., "Quasi-direct drive for low-cost compliant robotic manipulation," in *Proc. IEEE Int. Conf. Robot. Auto.*, 2019, pp. 437–443.

[4] T. Laliberté, M. Abdallah, and C. Gosselin, "A backdrivable 6-dof parallel robot for sensorless dynamically interactive tasks," *Robotics and Computer-Integrated Manufacturing*, vol. 86, p. 102642, 2024.

[5] A. Albu-Schäffer et al., "The DLR lightweight robot: design and control concepts for robots in human environments," *Industrial Robot: an international journal*, vol. 34, no. 5, pp. 376–385, 2007.

[6] K. Wen et al., "A backdrivable kinematically redundant (6+ 3)-degree-of-freedom hybrid parallel robot for intuitive sensorless physical human–robot interaction," *IEEE Trans. Robot.*, vol. 37, no. 4, pp. 1222–1238, 2020.

[7] C. Gosselin and L.-T. Schreiber, "Kinematically redundant spatial parallel mechanisms for singularity avoidance and large orientational workspace," *IEEE Trans. Robot.*, vol. 32, no. 2, pp. 286–300, 2016.

[8] C. Gosselin, T. Laliberté, and A. Veillette, "Singularity-free kinematically redundant planar parallel mechanisms with unlimited rotational capability," *IEEE Trans. Robot.*, vol. 31, no. 2, pp. 457–467, 2015.

[9] A. Yiğit et al., "Kinematic analysis and design of a novel (6+3)-dof parallel robot with fixed actuators," in *Proc. IEEE Int. Conf. Robot. Autom.*, 2023, pp. 9693–9699.

[10] J. Kim and C. Gosselin, "A backdrivable axisymmetric kinematically redundant (6+ 3)-degree-of-freedom hybrid parallel manipulator," in *Proc. IEEE Int. Conf. Robot. Autom.*, 2024, pp. 8835–8841.

[11] K. Marlow et al., "Workspace analysis of two similar 3-dof axis-symmetric parallel manipulators," in *Proc. IEEE/RSJ Int. Conf. Intel. Robots and Syst.*, 2014, pp. 1690–1696.

[12] M. Isaksson, "A family of planar parallel manipulators," in *Proc. IEEE Int. Conf. Robot. Autom.*, 2011, pp. 2737–2744.

[13] S. Liu, "Etude et conception de petits robots industriels: réalisation du robot miniature "Colibri"," Ph.D. dissertation, EPFL, Lausanne, 1991.

[14] J.-P. Merlet, "Singular configurations of parallel manipulators and Grassmann geometry," *The International Journal of Robotics Research*, vol. 8, no. 5, pp. 45–56, 1989.

[15] I. A. Bonev, D. Zlatanov, and C. M. Gosselin, "Advantages of the modified Euler angles in the design and control of PKMs," 2002.

[16] L.-T. Schreiber and C. Gosselin, "Passively driven redundant spherical joint with very large range of motion," *Journal of Mechanisms and Robotics*, vol. 9, no. 3, 2017, Art. no. 031014.

[17] P. M. Wensing et al., "Proprioceptive actuator design in the mit cheetah: Impact mitigation and high-bandwidth physical interaction for dynamic legged robots," *IEEE Trans. Robot.*, vol. 33, no. 3, pp. 509–522, 2017.